An Fe60 tetrahedral cage: building nanoscopic molecular assemblies through cyanometallate and alkoxo linkers

J.-R. Jiménez, A. Mondal, L.-M. Chamoreau, P. Fertey, F. Tuna, M. Julve, Azzedine Bousseksou, R. Lescouëzec, L. Lisnard

An $\{Fe_{60}\}$ tetrahedral cage: building nanoscopic molecular assemblies through cyanometallate and alkoxo linkers.

J.-R. Jiménez,[a,b] A. Mondal,[a,b] L.-M. Chamoreau,[a,b] P. Fertey,[c] F. Tuna,[d] M. Julve,[e] A. Bousseksou,[f] R. Lescouëzec*[a,b] and L. Lisnard*[a,b]

[a.] Sorbonne Universités, UPMC Univ. Paris 06, UMR 8232, IPCM, F-75005, Paris. E-mail: rodrigue.lescouëzec@upmc.fr.
[b.] CNRS, UMR 8232, Institut Parisien de Chimie Moléculaire, F-75005, Paris, France.
[c.] Synchrotron SOLEIL, F-91192 Gif Sur Yvette, France.
[d.] School of Chemistry and Photon Science Institute, The University of Manchester, Oxford Road, M139PL, Manchester, UK.
[e.] Universitat de València, Instituto de Ciencia Molecular, C/ Catedrático José Beltrán 2,,46980 Paterna (València) Spain
[f.] Laboratoire de Chimie de Coordination, CNRS, UPR 8241, Route de Narbonne, 31077 Toulouse Cedex 04, France.

A nanoscopic $\{Fe_{60}\}$ coordination cage (ca. 3 nm) was prepared by the self assembly of a partially blocked tricyanidoferrate(III) complex and tris(alkoxo)-based iron(III) coordination motifs. This cage is a rare example of mixed cyanido/alkoxo-bridged high nuclearity complex and it exemplifies the great potential of this new synthetic route to generate uncommon molecular architectures using cyanometallates as metalloligands versus alkoxo-based polynuclear entities.

Introduction

The synthesis of nanosized polymetallic assemblies represents an appealing challenge in molecular science. Besides the reward that is found for synthetic chemists in creating unique architectures, such macromolecular entities may reveal attractive chemical or physical properties. Ligands having chalcogen atoms as donors occupy a prominent place in this field, by setting size record such as in the $\{Ag_{490}\}$ sulfido-cluster,[1] and by representing the largest family of polynuclear complexes, in particular with the oxo-ligand. The work by Müller *et al.* has afforded oxo-clusters of unmatched nuclearities, such as the $\{Mo_{368}\}$ isopolyanion where the inorganic polycondensation is driven through a fine control of pH, redox state, stoichiometry and type of counter-ions.[2] Pope and co-workers have shown that lacunary heteropolyoxotungstates can act as nucleophilic multidentate ligands towards metal ions affording impressive heterometallic compounds such as the $\{As_{12}W_{148}Ce_{16}\}$ complex through self-assembly processes.[3] This pioneering work has paved the way to a series of giant polynuclear compounds, the latest "record" being the $\{P_{32}W_{224}Mn_{40}\}$ complex reported by Kögerler and co-workers.[4] This latter example also illustrates another fruitful synthetic strategy that relies on the use of preformed 3d polynuclear motifs as reactants to build high-nuclearity polymetallic species. Following this approach, Christou and co-workers were able to prepare a $\{Mn_{84}\}$ "nano-wheel" from an acetato-$\{Mn_{12}\}$ building block.[5] Recently, Winpenny *et al*. reported the preparation of macromolecular entities –up to 60 metal centres– associating tailor-made polynuclear motifs acting as Lewis acids and bases.[6] Overall, the oxo ligand clearly dominates the chemistry of the high-nuclearity complexes. Nonetheless, relatively large polynuclear species and cages have been obtained using other classical bridging ligands such as the cyanide. In this case, the synthetic approach generally relies on the use of preformed anionic mononuclear complexes that are used as metalloligands towards partially-blocked cationic complexes. Although the nuclearity of the resulting cages remains limited, the self-assembly of stable building blocks makes the preparation of heterometallic species an easy task and it can offer a better geometrical control on the final architecture. The face-centered $\{Cr_8Ni_6\}$ cubic cage, obtained from the preformed *fac*-$[Cr(Me_3tacn)(CN)_3]$ unit (Me_3tacn = 1,4,7-trimethyl-1,4,7-triazacyclononane), illustrates well this approach.[7] As far as we are aware, the largest cyanide-based polynuclear compound to date is the $\{Fe_{42}\}$ cage that was recently reported by Sato *et al.*[8]

Taking advantage of both cyanide and oxo chemistry, we have recently started to explore the reactivity of (hydr)oxo-bridged polynuclear species toward the cyanide-based metalloligand *fac*-$[Fe(Tp)(CN)_3]^-$ [Tp = tris(pyrazolyl)borate].[9,10] Our first results along this line, concerned the synthesis and magneto-structural study of a discrete $\{Fe_4Co_{12}\}$ cubic cage and of a $\{Fe_2Cu_6\}_n$ two-dimensional (2D) network. Both

compounds display (hydr)oxo-centered trimetallic motifs as nodes that are connected by the cyanide metalloligand. Here we present a mixed oxo-cyanido $\{Fe_{60}\}$ coordination cluster issued from the reaction of the *fac*-$[Fe(Tp)(CN)_3]^-$ species with tris(alkoxo)-based polymetallic iron(III) compounds. Among the reported tris(alkoxo)-iron(III) complexes, we have selected the tetrametallic $[Fe_4(thme)_2Cl_6(nPrOH)_6]$ complex (H_3thme = 1,1,1-tris(hydroxymethyl)ethane),[11] which is one of the first two original $\{Fe_4\}$ star-like tris(alkoxo) compounds reported in 2004.[11,12] A larger family of homo- and heterometallic derivatives has followed where the single-molecule magnet behaviour (SMM) associated to the $\{M_4\}$ star-like motif was reported.[13] The complex of formula $[Fe_4(thme)_2Cl_6(nPrOH)_6]$ however differs drastically from the members of the family that have followed: it displays twelve terminally bound labile groups on the peripheral iron centres instead of the chelating ligands found in the other parent motifs. This structural feature positioned this iron cluster as an excellent candidate in our investigation of the use of polynuclear units as polymetallic Lewis acids toward cyanometallates as ligands.

Results and discussion

The polymetallic tris(alkoxo)-based iron(III) complexes were obtained from a methanolic stock solution of Fe^{3+}/$thme^{3-}$ (3:1 metal to ligand molar ratio; see Experimental Section). Its addition to a solution of $PPh_4[Fe^{III}(Tp)(CN)_3]\bullet H_2O$ (PPh_4^+ = tetraphenylphosphonium) in acetonitrile led to the formation of deep green octahedral crystals of formula $[\{Fe_6O(thme)_4Cl_3\}_4\{Fe_4(thme)_2Cl_2(MeOH)_2(H_2O)_4\}_6\text{-}\{Fe(Tp)(CN)_3\}_{12}]Cl_5\bullet 15MeOH\bullet 35H_2O$ (**1**) by slow evaporation of the resulting solution at room temperature. **1** is a tetrahedral nanocage of approx. 3 nm edges that results from the assembly of three types of subunits: four $\{Fe^{III}_6O(thme)_4Cl_3\}$ ($\{Fe_6\}$) hexametallic entities that define the tetrahedron corners, six $\{Fe^{III}_4(thme)_2Cl_2(MeOH)_2(H_2O)_4\}$ ($\{Fe_4\}$) tetrametallic motifs which are placed along the tetrahedron edges, and twelve tris-monodentate *fac*-$[Fe^{III/II}(Tp)(CN)_3]^{-/2-}$ metalloligands that link the $\{Fe_6\}$ polymetallic subunits to the $\{Fe_4\}$ ones, while capping the tetrahedron faces (Fig. 1).

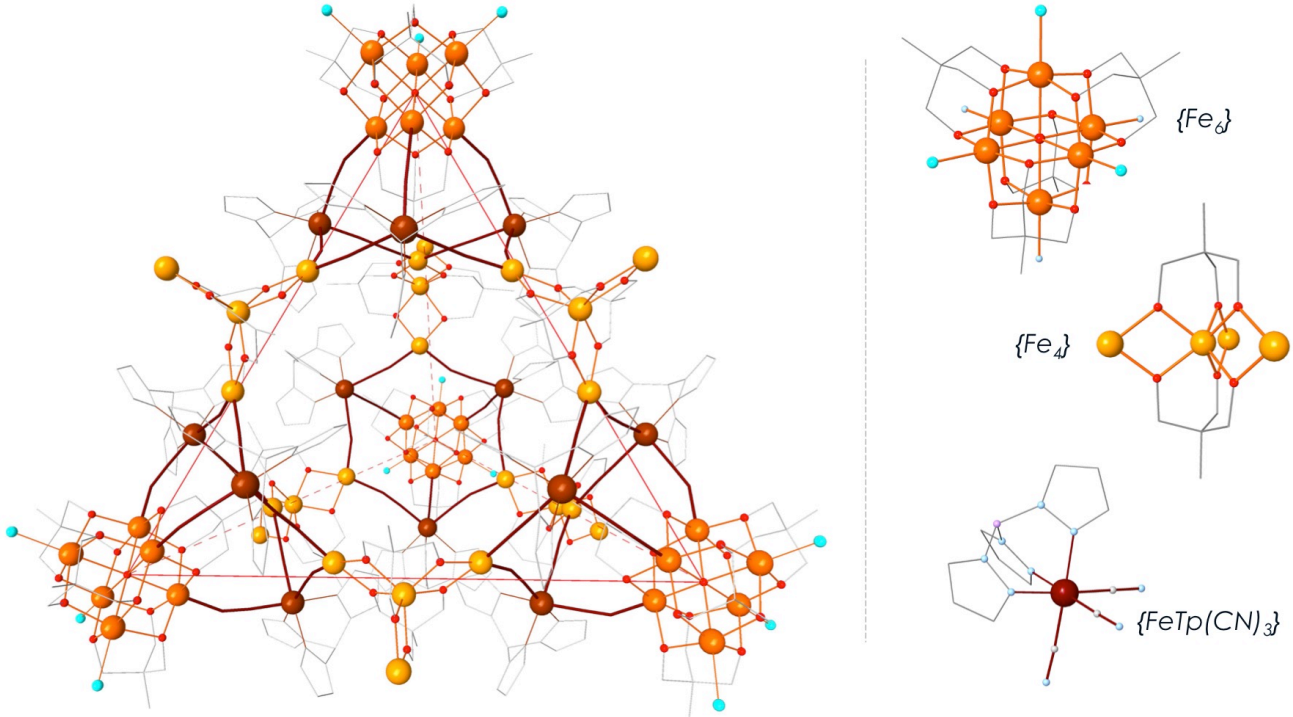

Fig. 1 Perspective drawing of **1** highlighting the tetrahedral architecture and its constitutive $\{Fe_6\}$, $\{Fe_4\}$ and $\{FeTp(CN)_3\}$ subunits. Colour code: orange, yellow and brown (Fe), red (O), cyan (Cl) and grey (C, B and N). Hydrogen atoms have been omitted for clarity.

The tetrahedron cavity is filled by a large cluster of hydrogen-bonded water molecules, which are anchored to the tetrahedral cage through hydrogen bonds with the coordinated water molecules of the $\{Fe_4\}$ fragments (see ESI†). If the presence of the $\{Fe_4\}$ was aimed at, the occurrence of the $\{Fe_6\}$ species was unexpected. Its presence in the starting solution cannot be excluded, so does its formation during

the reaction with the metalloligand. Performing the synthesis of **1** with a fresh or purposely aged (over two weeks) Fe^{3+}/$thme^{3-}$ solution causes no significant differences in the reaction yield.

In the $\{Fe_6\}$ subunit, six edge-sharing octahedral iron(III) ions are centred on a μ_6-oxygen atom and bridged by twelve μ-oxo groups coming from four capping $thme^{3-}$ ligands defining thus a Lindqvist isopolyoxometallate structure (Fig. 1). The latter is commonly observed for high oxidation state metal ions such as $Mo^{V/VI}$ or $V^{IV/V}$,[14] although examples of low-valent V^{III}, Cr^{III}, Mn^{III} or Fe^{III} Lindqvist structures were obtained in the presence of the stabilising tris(alkoxo) group.[15–18] Viewing the $\{Fe_6\}$ Lindqvist subunit as an octahedron, the $thme^{3-}$ ligands alternatively cap half of the polyhedron faces with their bridging oxo groups lying on the centre of each edge. The six terminal positions – i.e. the Lindqvist vertices – are coordinated, in a facial arrangement, by three chloride anions on one face and three nitrogen atoms from the cyanide bridges on the opposite one (Fig. 1 & 2a). The three cyanide ligands come from three $[Fe(Tp)(CN)_3]^{x-}$ entities (x = 1 and 2), each one having its two remaining cyanide groups connected to distinct $\{Fe_4\}$ units. As a result, each $[Fe(Tp)(CN)_3]^{x-}$ metalloligand is coordinated to one $\{Fe_6\}$ vertex and two distinct $\{Fe_4\}$ edges (Fig. 2b).

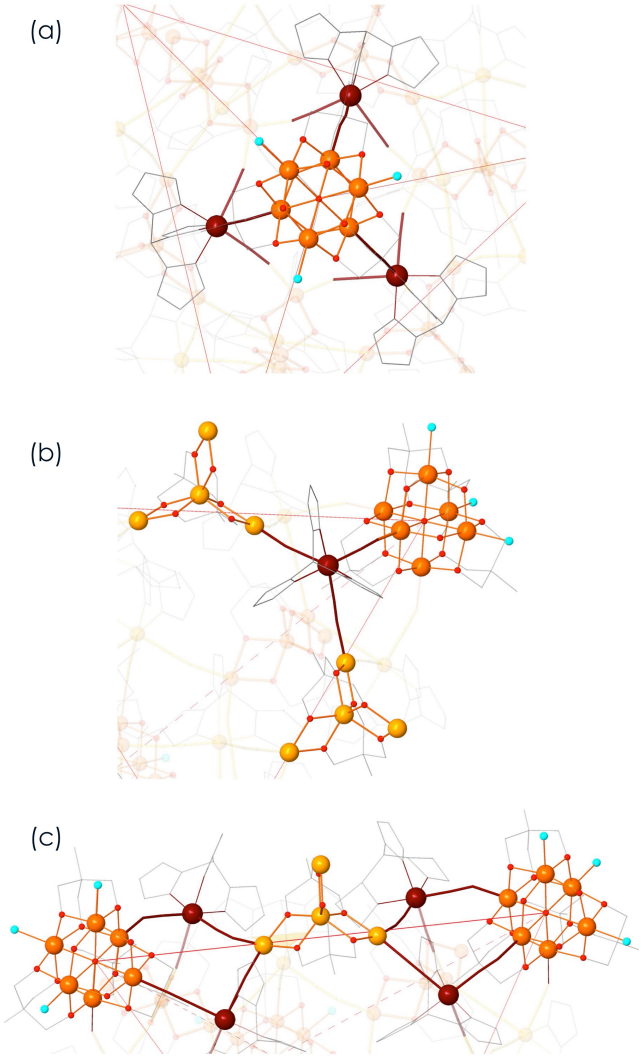

Fig. 2 Perspective views of fragments of **1** showing the connectivity between the constitutive $\{Fe_6\}$, $\{Fe_4\}$ and $\{Fe(Tp)(CN)_3\}$ subunits on the tetrahedron corner (a), on the tetrahedron face (b) and along the tetrahedron edge (c). Colour code: orange, yellow and brown (Fe), red (O), cyan (Cl) and grey (C, B and N). Hydrogen atoms have been omitted for clarity.

In the star-like $\{Fe_4\}$ subunit, one central iron(III) ion is coordinated to three peripheral iron atoms via six μ-alkoxo groups from two capping $thme^{3-}$ ligands that sit on each side of the plane of the iron atoms (Fig. 1). One of the peripheral iron(III) ions points outside of the tetrahedral entity whereas the other two lie on the tetrahedron edge. These ions are each *cis*-coordinated to two cyanide bridges from two $[Fe(Tp)(CN)_3]^{x-}$ linking units that are themselves connected to the same $\{Fe_6\}$ vertex. Overall, each $\{Fe_4\}$ subunit is linked to two adjacent $\{Fe_6\}$ apexes via four $[Fe(Tp)(CN)_3]^{x-}$ complexes, building so the edges of

the tetrahedral cage (Fig. 2c). Within the $\{Fe_4\}$ entities, the iron(III) ions linked to the $[Fe(Tp)(CN)_3]^{x-}$ metalloligands are six-coordinate with water/methanol molecules completing their coordination spheres. The external iron(III) ions are disordered onto two crystallographic positions and their coordination sphere is completed with solvents and/or chloride anions. The trigonal geometry of the $\{Fe_4\}$ units is only slightly distorted, with Fe–Fe–Fe angles along the tetrahedron edge ranging from 119 to 132°. The Fe–C–N angles in the $[Fe(Tp)(CN)_3]^{x-}$ metalloligands are fairly linear whereas the C–N–Fe angles are significantly bent (values in the ranges 174-179° and 152-171°, respectively; see ESI†). BVS calculations for the $\{Fe_4\}$ and the $\{Fe_6\}$ sub-units are consistent with iron(III) ions in the (alk)oxo-based motifs (see ESI†). The values of the Fe–C bond lengths do not allow to discriminate Fe(III) from Fe(II) in the $\{Fe(Tp)(CN)_3\}$ moieties. Indeed, the difference of bond distances for $Fe^{III/II}$ in the later complex is small (≈ 0.05 Å),[9,19,20] and our structural data resolution does not allow such a distinction.

However FT-IR spectroscopy clearly indicates the presence of both $\{Fe^{II}(Tp)(CN)_3\}$ and $\{Fe^{III}(Tp)(CN)_3\}$ units, pointing to a reduction of the cyanide metalloligand during the formation of **1**. Indeed, two weak cyanide stretching bands – that account for the presence of Fe^{III}-CN-Fe^{III} motifs[21] – are observed at 2158 and 2140 cm^{-1} together with the strong vibrations observed at 2092 and 2041 cm^{-1} that correspond to the Fe^{II}-CN-Fe^{III} cyanide bridges (see ESI†).[22,23]

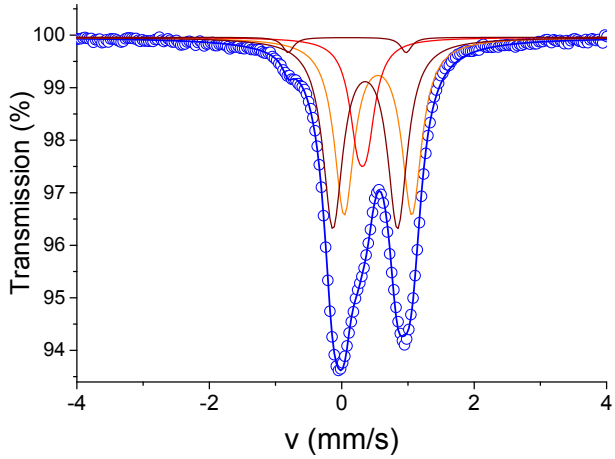

Fig. 3 Mössbauer spectrum of **1** at 80 K: experimental data (blue circles); best-fit (blue line); Fe^{III}_{HS} (orange and brown lines); Fe^{II}_{LS} (red line); Fe^{III}_{LS} (deep brown line).

The different environments and oxidation states of the iron ions have been confirmed with Mössbauer spectroscopy on crystals of **1** (Fig. 3). Three major components are clearly identified and the signals are well defined without any broadening. Two quadrupole doublets with typical parameters for Fe^{III}_{HS} (IS = 0.55 mm s^{-1}, ΔE_Q = 1.02 mm s^{-1} and IS = 0.35 mm s^{-1}, ΔE_Q = 0.98 mm s^{-1}) are ascribed to the twenty four iron ions of the four $\{Fe_6\}$ units and to the twenty four iron ions of the six $\{Fe_4\}$ motifs.[24] Their proportions (39.8 and 42.7%) match the expected one (40%). Another signal, with IS = 0.31 mm s^{-1}, ΔE_Q = 0.14 mm s^{-1} exhibits typical parameters of Fe^{II}_{LS} .[20,25] and it is ascribed to the $\{Fe^{II}(Tp)(CN)_3\}$ entities. It amounts to 15.6%, a percentage which is lower than the expected theoretical value (20%) if all $\{Fe^{III}(Tp)(CN)_3\}$ units were reduced. A fourth small signal, whose presence has been checked on a second crystalline sample, is clearly observed at IS = 0.08 mm s^{-1}, ΔE_Q = 1.78 mm s^{-1}. It is typical of Fe^{III}_{LS} ions and represents 1.9%, so that altogether the Fe^{II}_{LS} and Fe^{III}_{LS} amounts to 17.5%. This shows that most of the $[Fe^{III}(Tp)(CN)_3]^-$ species were reduced during the synthesis, so that –on average– only approximately one metalloligand per molecule remains unreduced.‡ The reduction of the $[Fe^{III}(Tp)(CN)_3]^-$ complex upon its reaction with metal salts has already been observed.[9,26] In fact, it is known that the redox potential of cyanometallates increases upon coordination.[22,23,26] In the present case, we assume that the coordination of strong Lewis acids (the Fe^{III} ions) to the cyanide-nitrogen atom facilitates the reduction of the cyanometallate unit by the methanol solvent.

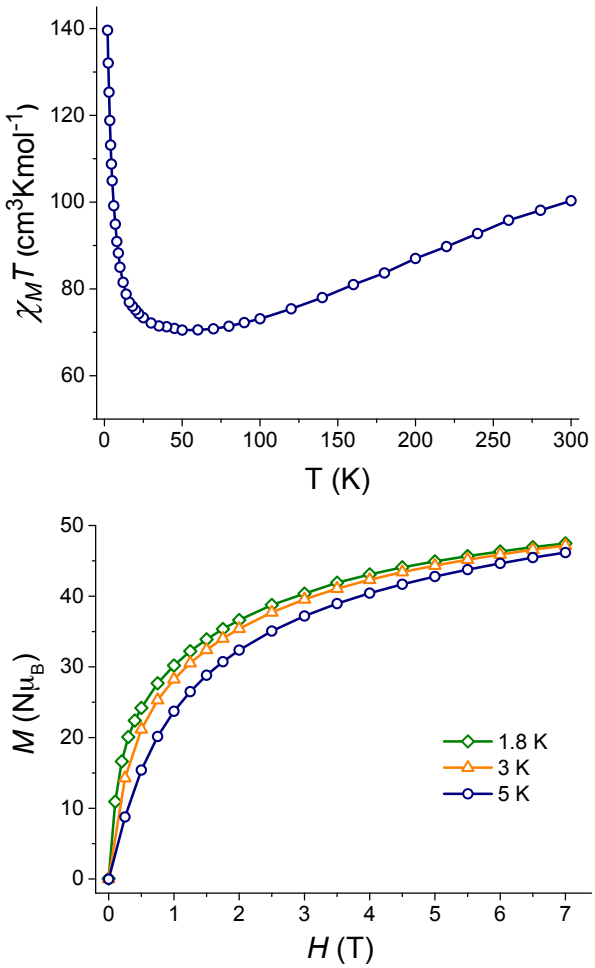

Fig. 4 (Top) Temperature dependence of the $\chi_M T$ product of **1** under applied dc fields of 1 T ($50 \leq T \leq 300$ K) and 0.01 T ($T < 50$ K). (Bottom) Field dependence of the magnetisation of **1** at 1.8, 3.0 and 5.0 K.

Finally, variable-temperature magnetic susceptibility and magnetisation measurements have been performed on **1** (Fig. 4 and see ESI†). The $\chi_M T$ *vs.* T plot (χ_M is the molar magnetic susceptibility, i.e. per sixty iron ions) exhibits a continuous decrease upon cooling from 300 to 100 K, because of the strong antiferromagnetic interactions within the {Fe_4} and {Fe_6} subunits. Given that no magnetic interactions are expected to occur between these subunits because of the presence of reduced {$Fe^{II}(Tp)(CN)_3$} *diamagnetic* linkers, S = 5 and S = 0 ground spin states would be achieved respectively,[11,18] and an increase of $\chi_M T$ would be predicted at very low temperatures. Indeed, the value of $\chi_M T$ exhibit a minimum of *ca.* 70 cm^3 mol^{-1} K between 90 and 50 K, and it increases rapidly afterwards to reach 140 cm^3 mol^{-1} K at 1.8 K. The isothermal *M vs. H* curves of **1** do not show any sign of saturation up to 7 T (Fig. 4 bottom). The fact that the *M* against *H/T* curves measured for different temperatures do not superpose, is indicative of a large magnetic anisotropy in **1** (see ESI†). This agrees with previous reports on {Fe_4} which have shown that there is an appreciable axial magnetic anisotropy (*D*) within the S = 5 spin state (D = -0.33 cm^{-1}).[11] It deserves to be noted that the existence of low-lying excited states due to weak inter- and/or intramolecular interactions could also be responsible for the non-superimposition of the isofield curves. Unfortunately, the crystal data of **1** do not permit a thorough examination of the possible intermolecular interactions. The low and diffuse electronic density precludes clear residues assignment and localisation of solvent molecules and counter-ions. Besides, given the complexity of the system and the many possible exchange pathways, the fit of the magnetic data would only be possible with over-parameterisation, yielding thus an unreliable model.

Conclusions

Complex **1** is a rare example of mixed cyanide/oxo(alkoxo)-based polynuclear assembly and it also represents a structurally unique example of high-nuclearity compound obtained from a metalloligand. It

compares well with the remarkable macromolecules prepared by Scheer and co-workers from an organometallic metalloligand,[34,35] and it actually sets a nuclearity record considering the cyanide-based assembling metalloligands.[8,36] A striking feature in **1** is the presence of two *distinct* tris(alkoxo)-based polynuclear motifs that have serendipitously assembled with the $[Fe(Tp)(CN)_3]^-$ building blocks. More importantly, the synthesis of the $\{Fe_{60}\}$ complex proves that the self-assembly of polynuclear units and cyanometallates is an efficient route towards uncommon polymetallic assemblies, including high-nuclearity cages. Given the diversity of accessible building blocks – from both cyanide and oxo families – original architectures and interesting chemical and physical properties can be expected in exploring further this synthetic route.

Experimental

Materials and methods

Preparation of the Fe^{3+}/$thme^{3-}$ solution. The methanolic solution was prepared following the first step of the reported procedure for the $[Fe_4(thme)Cl_6(nPrOH)_6]$ polymetallic complex[11] and starting from 3.0 g of anhydrous $FeCl_3$. The volume was adjusted to 100 mL, yielding a 0.18 M solution in iron(III).

Synthesis of 1. 7.5 mL of the Fe^{3+}/$thme^{3-}$ solution [1.38 mmol of iron(III)] previously diluted with an equivalent volume of methanol was added dropwise to an acetonitrile solution (10 mL) of $PPh_4[Fe(Tp)(CN)_3]\bullet H_2O$[27] (79.0 mg, 0.11 mmol). The resulting dark green solution was stirred for 20 min at room temperature, filtered and left to stand at room temperature. Slow evaporation of the solvent yielded dark crystals of **1** in ten days. They were collected by filtration, washed by sonication in acetonitrile and dried in air. Yield: 37 mg (31% based on $[Fe(Tp)(CN)_3]^-$). Elemental analysis calculated (%) for $C_{311}H_{598}B_{12}Cl_{29}Fe_{60}N_{108}O_{174}$ (M = 13143.2 g mol^{-1}): C, 28.42; H, 4.58; N, 11.51; Fe, 25.49; Cl, 7.82. Found: C, 28.50; H, 4.15; N, 11.21; Fe, 25.45; Cl, 6.52. IR (ATR cm^{-1}, see ESI† as well): 3356b, 2959w, 2913w, 2866m, 2490w, 2158w, 2140w, 2092m, 2041s, 1622m, 1502m, 1461m, 1430w, 1409s, 1401s, 1314s, 1214s, 1116s, 1074w, 1043s, 1017s, 919w, 823w, 789w, 762m, 716m, 689w, 663w; 598m, 514s, 469s, 437m and 386m.

Magnetic measurements. Variable-temperature magnetic measurements in dc mode were performed on polycrystalline samples of **1** restrained within a capsule in eicosane with a Quantum Design MPMS SQUID. Magnetic susceptibility data were corrected for the diamagnetism of the constituent atoms by using the Pascal's constants. The diamagnetism of the sample holder was measured and subtracted from the raw data.

IR Characterisation and Thermal Study. ATR/FT-IR spectra were collected on a Bruker TENSOR 27 equipped with a simple reflexion ATR diamond plate of the Harrick MPV2 series whereas the **FT-IR** (KBr) spectra were collected on a JASCO FT/IR-4100 spectrometer. The thermogravimetric analysis **(TGA)** was performed on a TA Instruments SDTQ600 under air with a heating rate of 5 °C/min.

Mössbauer Spectroscopy. The ^{57}Fe Mössbauer spectrum has been recorded at 80 K using a conventional constant-acceleration-type spectrometer equipped with a 50 mCi ^{57}Co source. Least-squares fitting of the Mössbauer spectrum has been carried out with the assumption of Lorentzian line shapes using the Recoil software package.

Crystallography. Crystal data for **1** ($C_{310}H_{596}B_{12}Cl_{28}Fe_{60}N_{108}O_{174}$): dark blocks, tetragonal, space group $I4_1/a$, a = 42.8834(4) Å, c = 83.8716(10) Å, V = 154260(3) Å^3, Z = 8, T = 100(2) K, ρ = 1.115 g cm^{-3}, F(000) = 53056, μ = 1.032 mm^{-1}. The data collection for **1** was carried out at the CRISTAL beamline (synchrotron SOLEIL, Paris) using the synchrotron radiation source (λ = 0.6683 Å). The temperature of the data collection (T = 100 K) was reached with a gas streamer (CryoIndustries of America), crystal-to-detector distance of 80 mm. The wavelength was selected with a double crystal monochromator (Si 111 crystals) and sagittal (horizontal) focalisation was achieved by bending the second crystal of the monochromator. The beam attenuation was performed using Al (or Cu) foils of different thicknesses inserted in the incident beam. Data collection strategies were generated with the CrysAlisPro CCD package. The refinement of the unit cell parameters and data reduction were carried out with CrysAlisPro RED.[28] After the absorption correction, the measured reflections were sorted, scaled and merged by using the SORTAV program.[29,30] The structure was solved with SHELXS-97[31] and refined with the SHELXL-2014/7 program[32] (WinGX software package[33]).

Data refinement gives (using 3340 parameters and 4494 restraints) $wR_2 = 0.3249$ (20654 unique reflections up to 1.3 Å resolution), $R_1 = 0.0947$ [14233 reflections with $I > 2\sigma(I)$], and *GOF* = 1.047. A general rigid bond restraint was applied to the entire structural model (RIGU instruction) due to low resolution. Some Tp ligands were geometrically restrained (distances), especially the ones disordered over two orientations. Two thme ligands needed quite a few restraints to get the refinement converging. The peripheral part of the {Fe_4} clusters was difficult to determine because of confused and low or even absent residual electron density in these external regions. Geometrical features, particularly distances, oriented our choices for the atom type assignment. However, the coordination spheres of the external iron atoms remain incomplete since no reliable model could be elected. We thus decided to leave the model as it is. Some solvent molecules nearby the {Fe_{60}} were localised; however large voids remain in the model, which might be filled with ions and solvent molecules. The data are insufficient to identify residual density in these regions. CCDC-1409712 contains the supplementary crystallographic data. These data can be obtained free of charge via www.ccdc.cam.ac.uk/conts/retrieving.html (or from the Cambridge Crystallographic Data Centre, 12 Union Road, Cambridge CB21EZ, UK; fax: (+44) 1223-336033; or deposit@ccdc.cam.uk).

Acknowledgements

This work was supported by the Centre National de la Recherche Scientifique (CNRS, France), the Ministère de l'Enseignement Supérieur et de la Recherche (MESR, France) and the Generalitat Valenciana (PROMETEOII/204/70 and ISIC/2012/002). We acknowledge the CNRS PICS programme (07345, VALPARESEAU project), SOLEIL for provision of synchrotron radiation facilities at the CRISTAL beamline (Proposal 20120026) and the EPSRC UK National EPR Research Facility and Service at the University of Manchester. We are grateful to Jean-François Meunier for his help in measuring the Mössbauer spectra.

Notes and references

‡ XRD data do not allow the identification of a specific iron(III) site among the six {Fe(Tp)} groups of the asymmetric unit.

1 O. Fuhr, S. Dehnen and D. Fenske, *Chem. Soc. Rev.*, 2013, **42**, 1871–1906.
2 A. Müller and P. Gouzerh, *Chem. Soc. Rev.*, 2012, **41**, 7431–7463.
3 K. Wassermann, M. H. Dickman and M. T. Pope, *Angew. Chem., Int. Ed. Engl.*, 1997, **36**, 1445–1448.
4 X. Fang, P. Kögerler, Y. Furukawa, M. Speldrich and M. Luban, *Angew. Chem., Int. Ed.*, 2011, **50**, 5212–5216.
5 A. J. Tasiopoulos, A. Vinslava, W. Wernsdorfer, K. A. Abboud and G. Christou, *Angew. Chem., Int. Ed.*, 2004, **43**, 2117–2121.
6 G. F. S. Whitehead, F. Moro, G. A. Timco, W. Wernsdorfer, S. J. Teat and R. E. P. Winpenny, *Angew. Chem., Int. Ed.*, 2013, **52**, 9932–9935.
7 P. A. Berseth, J. J. Sokol, M. P. Shores, J. L. Heinrich and J. R. Long, *J. Am. Chem. Soc.*, 2000, **122**, 9655–9662.
8 S. Kang, H. Zheng, T. Liu, K. Hamachi, S. Kanegawa, K. Sugimoto, Y. Shiota, S. Hayami, M. Mito, T. Nakamura, M. Nakano, M. L. Baker, H. Nojiri, K. Yoshizawa, C. Duan and O. Sato, *Nat Commun*, 2015, **6**, 5955.
9 A. Mondal, S. Durdevic, L.-M. Chamoreau, Y. Journaux, M. Julve, L. Lisnard and R. Lescouezec, *Chem. Commun.*, 2013, **49**, 1181–1183.
10 A. Mondal, P.-I. Dassie, L.-M. Chamoreau, Y. Journaux, M. Julve, L. Lisnard and R. Lescouezec, *Cryst. Growth Des.*, 2013, **13**, 4190–4194.
11 M. Moragues-Cánovas, E. Rivière, L. Ricard, C. Paulsen, W. Wernsdorfer, G. Rajaraman, E. K. Brechin and T. Mallah, *Adv. Mater.*, 2004, **16**, 1101–1105.
12 A. Cornia, A. C. Fabretti, P. Garrisi, C. Mortalo, D. Bonacchi, D. Gatteschi, R. Sessoli, L. Sorace, W. Wernsdorfer and A.-L. Barra, *Angew. Chem., Int. Ed.*, 2004, **43**, 1136–1139.
13 P. Totaro, K. C. M. Westrup, M.-E. Boulon, G. G. Nunes, D. F. Back, A. Barison, S. Ciattini, M. Mannini, L. Sorace, J. F. Soares, A. Cornia and R. Sessoli, *Dalton Trans.*, 2013, **42**, 4416–4426; and references therein.
14 M. T. Pope, *Heteropoly and Isopoly Oxometalates*, Springer-Verlag GmbH, 1983.
15 K. Hegetschweiler, H. Schmalle, H. M. Streit and W. Schneider, *Inorg. Chem.*, 1990, **29**, 3625–3627.
16 A. Cornia, D. Gatteschi, K. Hegetschweiler, L. Hausherr-Primo and V. Gramlich, *Inorg. Chem.*, 1996, **35**, 4414–4419.
17 T. C. Stamatatos, K. V. Pringouri, K. A. Abboud and G. Christou, *Polyhedron*, 2009, **28**, 1624–1627.
18 L. J. Batchelor, R. Shaw, S. J. Markey, M. Helliwell and E. J. L. McInnes, *Chem. - Eur. J.*, 2010, **16**, 5554–5557.
19 A. Mondal, Y. Li, M. Seuleiman, M. Julve, L. Toupet, M. Buron-Le Cointe and R. Lescouëzec, *J. Am. Chem. Soc.*, 2013, 1653–1656.
20 M. Nihei, Y. Sekine, N. Suganami, K. Nakazawa, A. Nakao, H. Nakao, Y. Murakami and H. Oshio, *J. Am. Chem. Soc.*, 2011, **133**, 3592–3600.
21 R. Lescouëzec, J. Vaissermann, F. Lloret, M. Julve and M. Verdaguer, *Inorg. Chem.*, 2002, **41**, 5943–5945.
22 P. V. Bernhardt, F. Bozoglian, B. P. Macpherson and M. Martinez, *Coord. Chem. Rev.*, 2005, **249**, 1902–1916.
23 J.-D. Cafun, G. Champion, M.-A. Arrio, C. C. dit Moulin and A. Bleuzen, *J. Am. Chem. Soc.*, 2010, **132**, 11552–11559.

24 P. S. Ammala, S. R. Batten, J. D. Cashion, C. M. Kepert, B. Moubaraki, K. S. Murray, L. Spiccia and B. O. West, *Inorganica Chimica Acta*, 2002, **331**, 90–97.
25 A. Mondal, Y. Li, P. Herson, M. Seuleiman, M.-L. Boillot, E. Rivière, M. Julve, L. Rechignat, A. Bousseksou and R. Lescouëzec, *Chem. Commun.*, 2012, **48**, 5653–5655.
26 M. Nihei, M. Ui, N. Hoshino and H. Oshio, *Inorg. Chem.*, 2008, **47**, 6106–6108.
27 R. Lescouëzec, J. Vaissermann, F. Lloret, M. Julve and M. Verdaguer, *Inorg. Chem.*, 2002, **41**, 5943–5945.
28 *CrysAlisPro CCD and CrisAlisPro RED*, Oxford Diffraction Ltd., Yarnton, Oxfordshire, U.K., 2009.
29 R. H. Blessing, *Crystallogr. Rev.*, 1987, **1**, 3.
30 R. H. Blessing, *Acta Crystallogr., Sect. A*, 1995, **51**, 33.
31 G. M. Sheldrick, *Acta Crystallogr., Sect. A*, 2008, **64**, 112.
32 G. M. Sheldrick, *Acta Crystallogr., Sect. C*, 2015, **71**, 3–8.
33 L. J. Farrugia, *J. Appl. Crystallogr.*, 1999, **32**, 837.
34 J. Bai, A. V. Virovets and M. Scheer, *Science*, 2003, **300**, 781–783.
35 C. Heindl, E. V. Peresypkina, A. V. Virovets, W. Kremer and M. Scheer, *J. Am. Chem. Soc.*, 2015, **137**, 10938–10941.
36 X.-Y. Wang, A. V. Prosvirin and K. R. Dunbar, *Angew. Chem., Int. Ed.*, 2010, **49**, 5081–5084.

Supplementary information for:

An {Fe_{60}} tetrahedral cage: building nanoscopic molecular assemblies through cyanometallate and alkoxo linkers

Juan-Ramón Jiménez, Abhishake Mondal, Lise-Marie Chamoreau, Pierre Fertey, Floriana Tuna, Miguel Julve, Azzedine Bousseksou, Rodrigue Lescouëzec* and Laurent Lisnard*

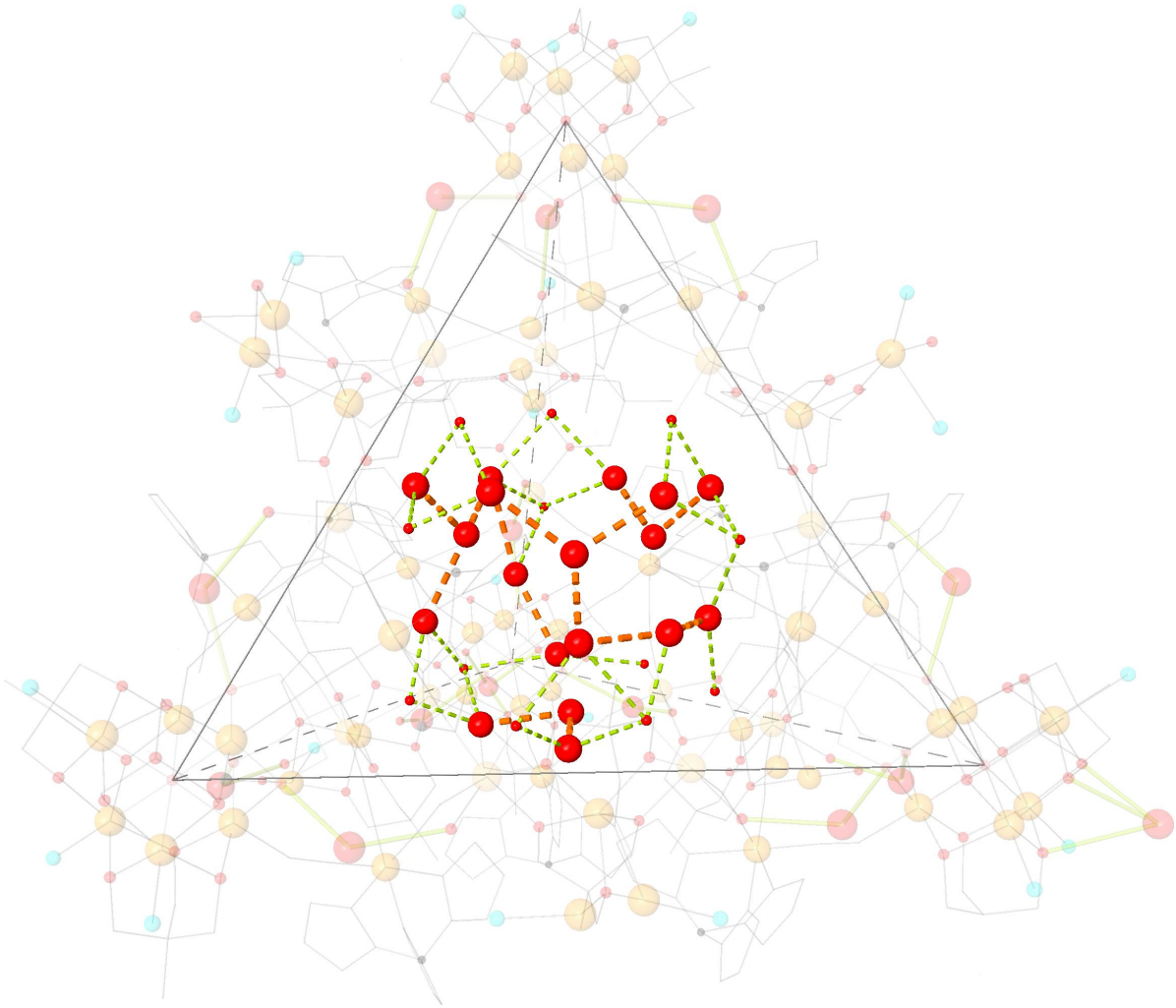

Figure S1. View of the water molecules hosted in the tetrahedron cavity. Colour code: orange, yellow and brown (Fe), red (O), cyan (Cl) and grey (C, B and N). Hydrogen atoms have been omitted for clarity. Dotted lines indicate H-bonds: orange (within the water motif) and green (involving an oxygen atom from the cage).

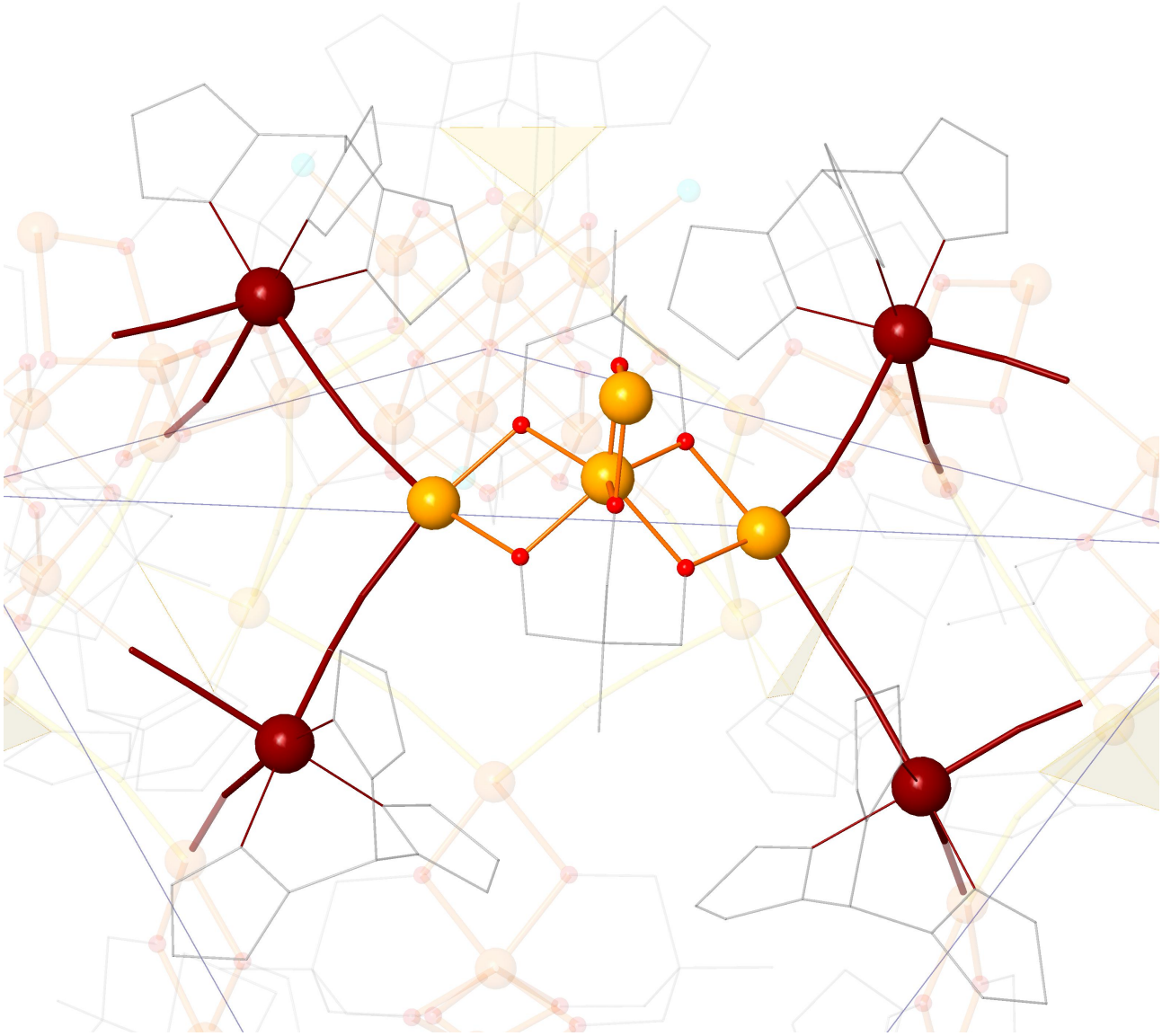

Figure S2. Representation of the {Fe_4} star-like subunit in **1** and of its connectivity with the {FeTp} units. Colour code: orange, yellow and brown (Fe), red (O), cyan (Cl) and grey (C, B and N). Hydrogen atoms have been omitted for clarity.

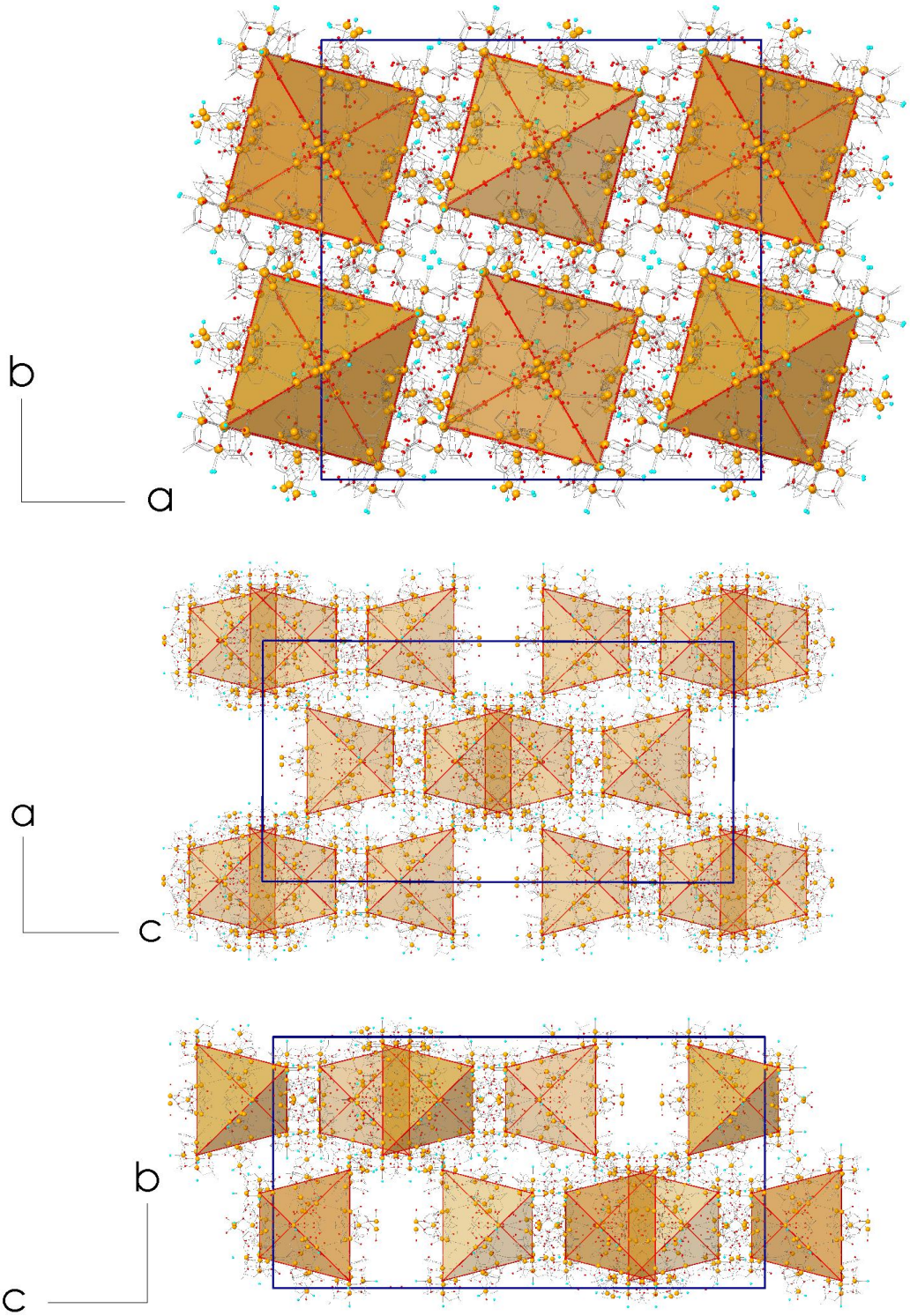

Figure S3. Crystal packing of **1** along the crystallographic *a* (a), *b* (b) and *c* (c) axes with a polyhedral view of the {Fe_{60}} tetrahedral cages. Colour code: light orange (Fe), red (O), cyan (Cl) and grey (C, B and N). Hydrogen atoms have been omitted for clarity.

Table S1. Selected bond distances (Å) and angles (°) in **1**

{Fe_6}	Fe—O	2.05 [1.96(1) – 2.32(1)]	X–Fe–X (X: Cl, N, O)	89.6 [80.3(3) – 100.4(4)]
	Fe—N	2.03 [2.00(2) – 2.05(1)]	Fe–(μ_6-O)–Fe	89.9 [89.2(5) – 91.6(5)]
	Fe—Cl	2.2 [2.263(3) – 2.287(7)]		
{Fe_4}*	Fe—O	2.0 [1.91(2) – 2.16(2)]	Fe–Fe–Fe	119.0 [100.1(3) – 132.2(2)]
	Fe—N	2.02 [1.99(2) – 2.06(2)]		
{FeTp}	Fe—C	1.85 [1.79(3) – 1.92(2)]	X–Fe–X (X: C, N)	89 [72(1) – 101(1)]
	Fe—N	1.99 [1.85(2) – 2.15(4)]	Fe–C–N	177 [174(1) – 179(2)]
			C–N–Fe(∈{Fe_6}/{Fe_4})	163 [152.5(1) – 171(2)]

**The values of the distances and angles around the peripheral iron atoms (Fe24, Fe34, Fe54 and Fe72) have been excluded from the analysis because of the uncertainty on the environment for these atoms.*

Table S2. BVS calculations[1–3]

{Fe_6}	Calc. for Fe(II)	Calc. for Fe(III)	{Fe_4}*	Calc. for Fe(II)	Calc. for Fe(III)
Fe1	2,73	2,89	Fe21	2,69	2,89
Fe2	2,76	2,92	Fe22	3,13	3,26
Fe3	2,82	2,99	Fe23	2,69	2,89
Fe4	2,76	2,90			
Fe5	2,72	2,85	Fe31	2,83	3,04
Fe6	2,72	2,85	Fe32	3,09	3,22
Fe7	2,78	2,92	Fe33	2,82	3,03
Fe8	2,73	2,88			
Fe9	2,70	2,86	Fe51	2,84	3,05
Fe10	2,71	2,85	Fe52	3,05	3,17
Fe11	2,75	2,89			
Fe12	2,73	2,87	Fe70	2,75	2,96
			Fe71	2,97	3,09

**The values of the distances around the peripheral iron atoms (Fe24, Fe34, Fe54 and Fe72) have been omitted from the calculations because of the uncertainty on the environment for these atoms.*

1 I. D. Brown and D. Altermatt, *Acta Crystallogr., Sect. B*, 1985, **41**, 244–247.
2 N. E. Brese and M. O'Keeffe, *Acta Crystallogr., Sect. B*, 1991, **47**, 192–197.
3 M. O'Keeffe and N. E. Brese, *Acta Crystallogr., Sect. B*, 1992, **48**, 152–154.

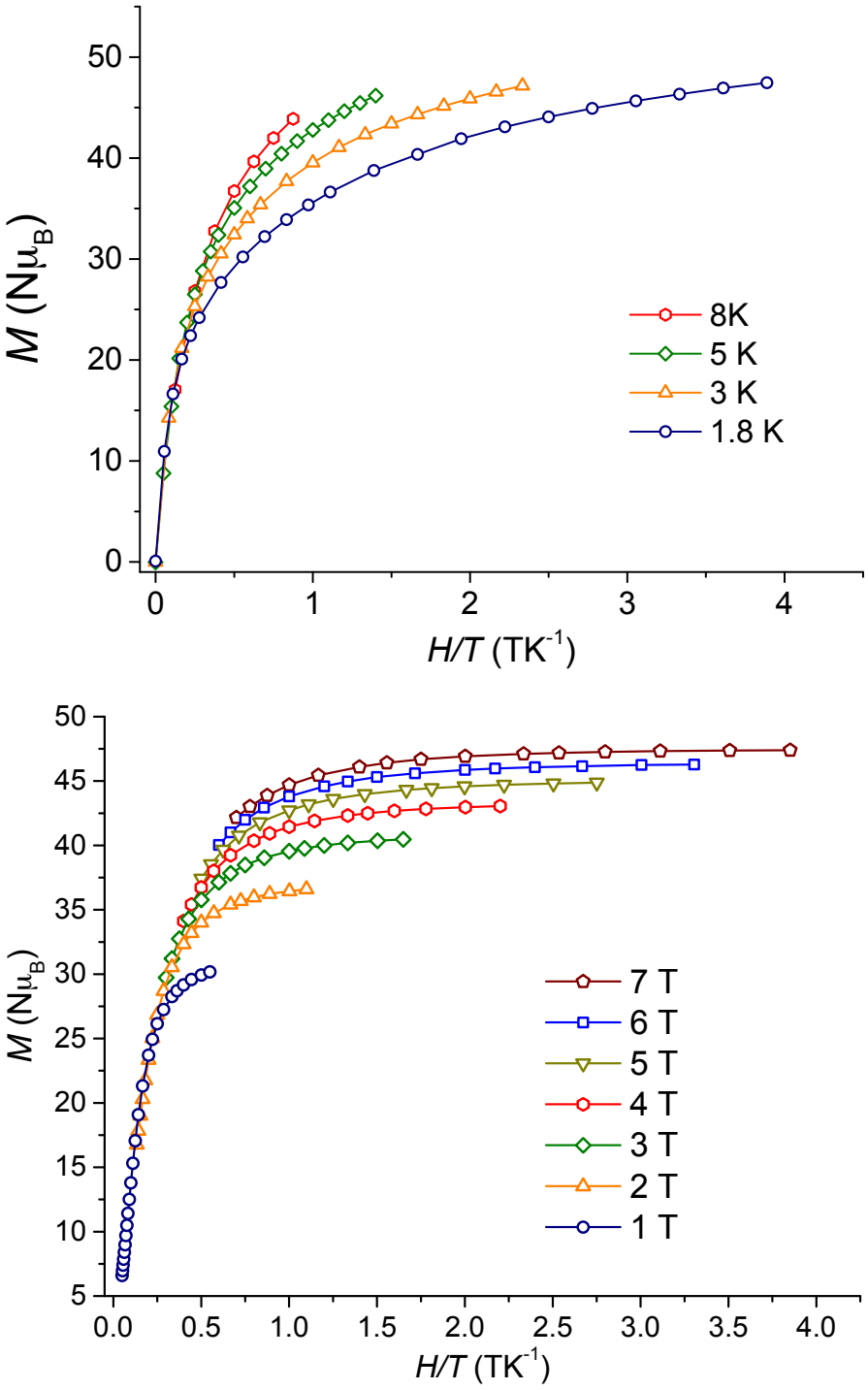

Figure S4. Field dependence of the magnetization of **1** at 1.8, 3.0 and 5.0 K; isothermal and isofield reduced magnetization of **1**.

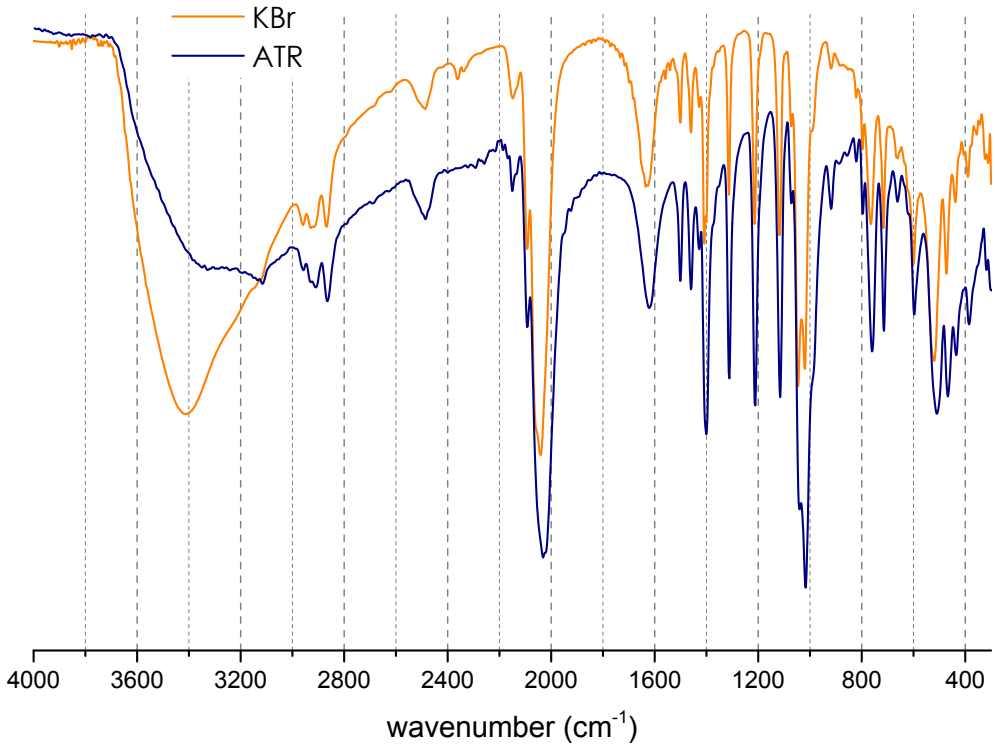

Figure S5. FT-IR spectra of **1** obtained by ATR (blue) and on KBr pellet (orange).

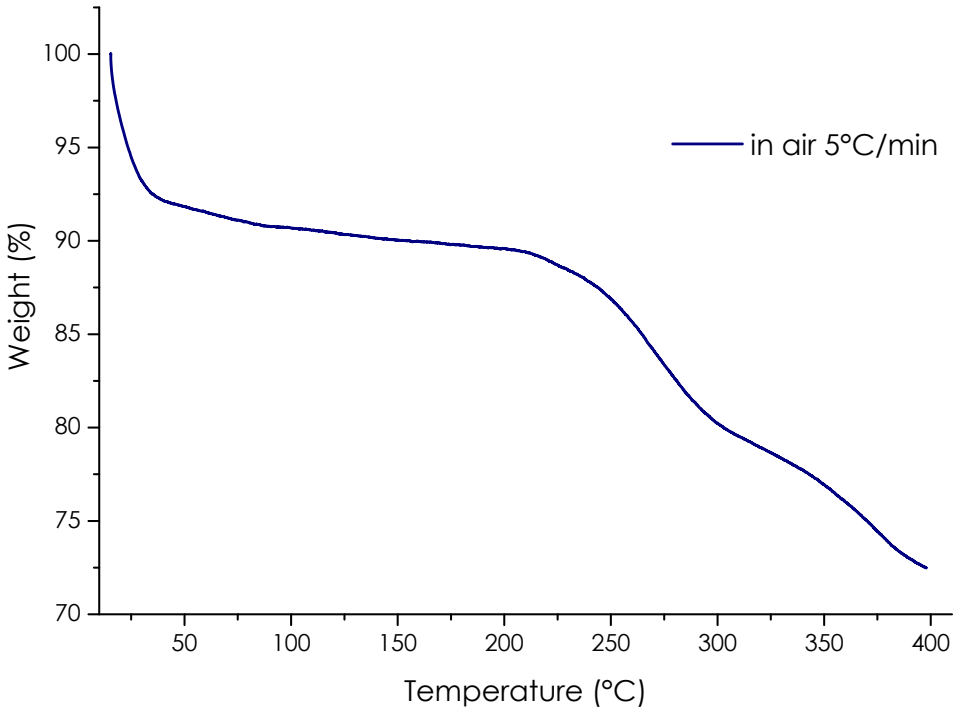

Figure S6. Thermogravimetric analysis of **1** in air at a heating rate of 5 °C/min.